Multiparameter full-waveform inversion for isotropic acoustic media

Yinbin Ma, Musa Maharramov, Robert Clapp, and Biondo Biondi

ABSTRACT

We implement multiparameter full-waveform inversion (FWI) in the isotropic acoustic media with the nonlinear conjugate gradient (CG) method. The performance of the FWI is evaluated using different combinations of acoustic parameters, including velocity, density and acoustic impedance. Simultaneous inversion of velocity and density leads to smoother results, when compared with the inversion results for velocity and acoustic impedance. We discuss the crosstalk between parameters for different parameterizations of FWI. We show the second order method can be used to reduce the crosstalk by applying the approximated inverse of the Hessian to the gradient.

INTRODUCTION

Full-waveform inversion (Tarantola, 1984; Virieux and Operto, 2009) is a challenging technique that estimates the high-resolution subsurface model by minimizing the mismatch between the observed data and the synthetic data. The first order derivative is needed for FWI, and the Hessian is used in Newton-based methods. It is known that the adjoint-state method is an efficient method to compute the Frechet derivative (Tromp et al., 2005; Plessix, 2006) and the Hessian (Fichtner, 2011; Fichtner and Trampert, 2011) for FWI.

FWI is a useful tool for time-lapse (4D) seismic imaging problems (Maharramov and Biondi, 2013). For this purpose, it is reasonable to use multiparameter FWI because both the velocity and density change during production. Geomechanical effects have been observed, which leads to change in the anisotropic and elastic parameters.

In this paper, we implement multiparameter FWI in the acoustic media with the nonlinear CG method (Nocedal and Wright, 2006; Maharramov and Biondi, 2013). Two acoustic parameters are estimated simultaneously. We discuss the crosstalk between different parameters, and test the feasibility of scaling/rotating the gradient using the approximated inverse of the Hessian.

The Marmousi model with non-constant density is used to test our implementation of the FWI. We first use the constant-density wave equation to fit the data by neglecting density variation. The effect of density leaks into the velocity model during the inversion. We test multiparameter FWI with different parameterizations (Operto

et al., 2013). The inversion results are smoother for the (v, ρ) parameterization when compared with the results for the (v, I_p) parameterization, where v is the velocity, ρ is the density and I_p is the acoustic impedance.

We study the crosstalk for (K, ρ), (V, ρ), and (V, I_p) parameterizations, where K is the bulk modulus. For (K, ρ), the gradients for K and ρ have similar amplitude. However we cannot distinguish the contribution from each parameter. Proper rotation of the gradients would improve the FWI results. For the (V, ρ) parameterization, the gradient for V has higher amplitude when compared with the gradient for ρ, and the FWI does not update the density model effectively unless we scale the gradient. To scale/rotate the gradient, we apply the approximated inverse of the Hessian using the CG method. The crosstalk is reduced significant after applying the approximated inverse of the Hessian to the gradient.

METHOD

We use the least-squares misfit function for FWI in the time domain (Tarantola, 1984) as follows:

$$J(m) = \frac{1}{2} \sum_r \int_0^T ||S_r \mathbf{u}(m) - d_r||_2^2 dt, \tag{1}$$

where S_r is the sampling operator for the receivers, d_r is the observed data at the receiver $\mathbf{r}$, $\mathbf{u}$ is the synthetic pressure wavefield, and m is the model parameter.

The pressure field $\mathbf{u}$ is computed using the acoustic approximation of the wave equation with a non-constant density, as follows:

$$\begin{cases} \left[\frac{1}{v^2\rho}\partial_t^2 - \tilde{\nabla} \cdot (\frac{1}{\rho}\nabla)\right] \mathbf{u} & = \mathbf{f} \\ \mathbf{u}(\mathbf{r}, t=0) & = 0 \\ \partial_t \mathbf{u}(\mathbf{r}, t=0) & = 0, \end{cases} \tag{2}$$

where v is the p-wave velocity, ρ is the density, and $\mathbf{f}$ is the source wavefield. Numerically, we solve Equation (2) in the time domain using a staggered-grid finite difference method, starting from $t = 0$ to maximum recording time $t = \mathrm{T}$.

We choose our model parameters as follows,

$$m_v \equiv \log(v/v_0), \tag{3}$$
$$m_\rho \equiv \log(\rho/\rho_0), \tag{4}$$
$$m_K \equiv \log(K/K_0), \tag{5}$$
$$m_{I_p} \equiv \log(I_p/I_{p0}), \tag{6}$$

where K is the bulk modulus and I_p is the acoustic impedance. v_0, ρ_0, K_0 and I_{p0} are the initial models. We can recover the physical parameters after the inversion, e.g., $v = v_0 \exp(m_v)$.

The wave equation can be parametrized by choosing any two of the model parameters: m_v, m_ρ, m_K, and m_I. Different parameterizations for elastic wave equation have been studied (Alves, 2015). The gradients for (m_K, m_ρ), (m_v, m_ρ) and (m_v, m_{I_p}) parameterizations can be computed as follows:

$$\frac{\partial J}{\partial(m_K, m_\rho)} = \begin{bmatrix} \frac{\partial J}{\partial m_K} \\ \\ \frac{\partial J}{\partial m_\rho} \end{bmatrix} = \begin{bmatrix} \frac{1}{K}\mathbf{I}_t(\lambda, u) \\ \\ -\frac{1}{\rho}\mathbf{I}_x(\lambda, u) \end{bmatrix}, \tag{7}$$

$$\frac{\partial J}{\partial(m_v, m_\rho)} = \begin{bmatrix} \frac{\partial J}{\partial m_v} \\ \\ \frac{\partial J}{\partial m_\rho} \end{bmatrix} = \begin{bmatrix} \frac{2}{v^2\rho}\mathbf{I}_t(\lambda, u) \\ \\ \frac{1}{v^2\rho}\mathbf{I}_t(\lambda, u) - \frac{1}{\rho}\mathbf{I}_x(\lambda, u) \end{bmatrix}, \tag{8}$$

and,

$$\frac{\partial J}{\partial(m_v, m_{I_p})} = \begin{bmatrix} \frac{\partial J}{\partial m_v} \\ \\ \frac{\partial J}{\partial m_{I_p}} \end{bmatrix} = \begin{bmatrix} \frac{1}{vI_p}\mathbf{I}_t(\lambda, u) + \frac{v}{I_p}\mathbf{I}_x(\lambda, u) \\ \\ \frac{1}{vI_p}\mathbf{I}_t(\lambda, u) - \frac{v}{I_p}\mathbf{I}_x(\lambda, u) \end{bmatrix}, \tag{9}$$

where we define two imaging operators as follows,

$$\mathbf{I}_t(u_1, u_2) \equiv \int_0^T u_1 \partial_t^2 u_2 dt, \tag{10}$$

$$\mathbf{I}_x(u_1, u_2) \equiv \int_0^T (\tilde{\nabla}^* u_1) \cdot (\nabla u_2)\, dt. \tag{11}$$

While the first-order methods suffer from crosstalk between parameters, the second-order methods can reduce the crosstalk. Suppose M is the model that we want to estimate, where M can be (m_v, m_ρ) or (m_v, m_{I_p}), etc. Then ΔM computed from Equation (12) has less crosstalk when compared with the gradient $\frac{\partial J}{\partial M}$,

$$H_M \Delta M = -\frac{\partial J}{\partial M}, \tag{12}$$

where H_M is the Hessian with respect to M. The expression of the Hessian for (m_K, m_ρ) parameters is as follows,

$$H_{(m_K, m_\rho)} \begin{bmatrix} \Delta m_K \\ \\ \Delta m_\rho \end{bmatrix} = \begin{bmatrix} \frac{1}{K}\left(F\mathbf{I}_t(\lambda, \delta u_1) + \mathbf{I}_t(\mu, u) - F\Delta m_K \mathbf{I}_t(\lambda, u)\right) \\ \\ \frac{1}{\rho}\left(-F\mathbf{I}_x(\lambda, \delta u_1) - \mathbf{I}_x(\mu, u) - F\Delta m_\rho \mathbf{I}_x(\lambda, u)\right) \end{bmatrix}, \tag{13}$$

where $F = 1$ for the full Hessian, and $F = 0$ for the Gauss-Newton Hessian. The Hessian for other parameterizations are readily obtained from $H_{(m_K, m_\rho)}$ by linear transformation because the Jacobian matrix is constant for different pairs of parameters,

$$H_{M_1} = G^T H_{M_2} G, \tag{14}$$
$$G = \frac{\partial M_1}{\partial M_2}. \tag{15}$$

The wavefields used in the expression for the gradient and the Hessian can be computed as follows,

$$[\frac{1}{v^2\rho}\partial_t^2 - \tilde{\nabla}\cdot(\frac{1}{\rho}\nabla)]u = f, \tag{16}$$
$$[\frac{1}{v^2\rho}\partial_t^2 - \tilde{\nabla}\cdot(\frac{1}{\rho}\nabla)]^*\lambda = \sum_r S_r^*(S_r u - d_r), \tag{17}$$
$$[\frac{1}{v^2\rho}\partial_t^2 - \tilde{\nabla}\cdot(\frac{1}{\rho}\nabla)]\delta u_1 = -\left(\frac{\partial L}{\partial m}\Delta m\right)u, \tag{18}$$
$$[\frac{1}{v^2\rho}\partial_t^2 - \tilde{\nabla}\cdot(\frac{1}{\rho}\nabla)]^*\mu_a = S_r^* S_r \delta u_1, \tag{19}$$
$$[\frac{1}{v^2\rho}\partial_t^2 - \tilde{\nabla}\cdot(\frac{1}{\rho}\nabla)]^*\mu_b = -\left(\frac{\partial L}{\partial m}\Delta m\right)^*\lambda. \tag{20}$$
$$\mu = \mu_a + F\mu_b \tag{21}$$

SINGLE PARAMETER FULL-WAVEFORM INVERSION

The FWI code is tested on the Marmousi model in this section. The true velocity model is shown in Figure 4(a) and the starting velocity model is shown in Figure 4(b). A constant density Marmousi model is used for the first numerical study. The same wave equation is used for both modeling and inversion. The limitation of our inversion results comes from the band-limited data and incomplete illumination coverage. The velocity is first estimated using the data with frequency centered at 5 Hz to avoid cycle skipping issues as shown in Figure 1(c). The final inversion result using the data centered at 30 Hz is shown in Figure 1(d). Figure 2 shows the data residual before and after fitting the data centered at 5 Hz. The data residual is reduced significantly except for the reflection from the deep corner caused by insufficient illumination from the diving wave.

When the true model contains density variation, we can attempt to fit the data by updating the model $(m_v, m_\rho = 0)$, where the density model is forced to be constant. The wave equation used for the inversion is simpler than the wave equation used for the modeling. The velocity model is used to predict the kinematics and reflectivity simultaneous by estimating,

$$v_{inversion} \approx v_{true}, \tag{22}$$
$$v_{inversion} \approx I_{p_{true}}/\rho_{water} = v_{true}\frac{\rho_{true}}{\rho_{water}}. \tag{23}$$

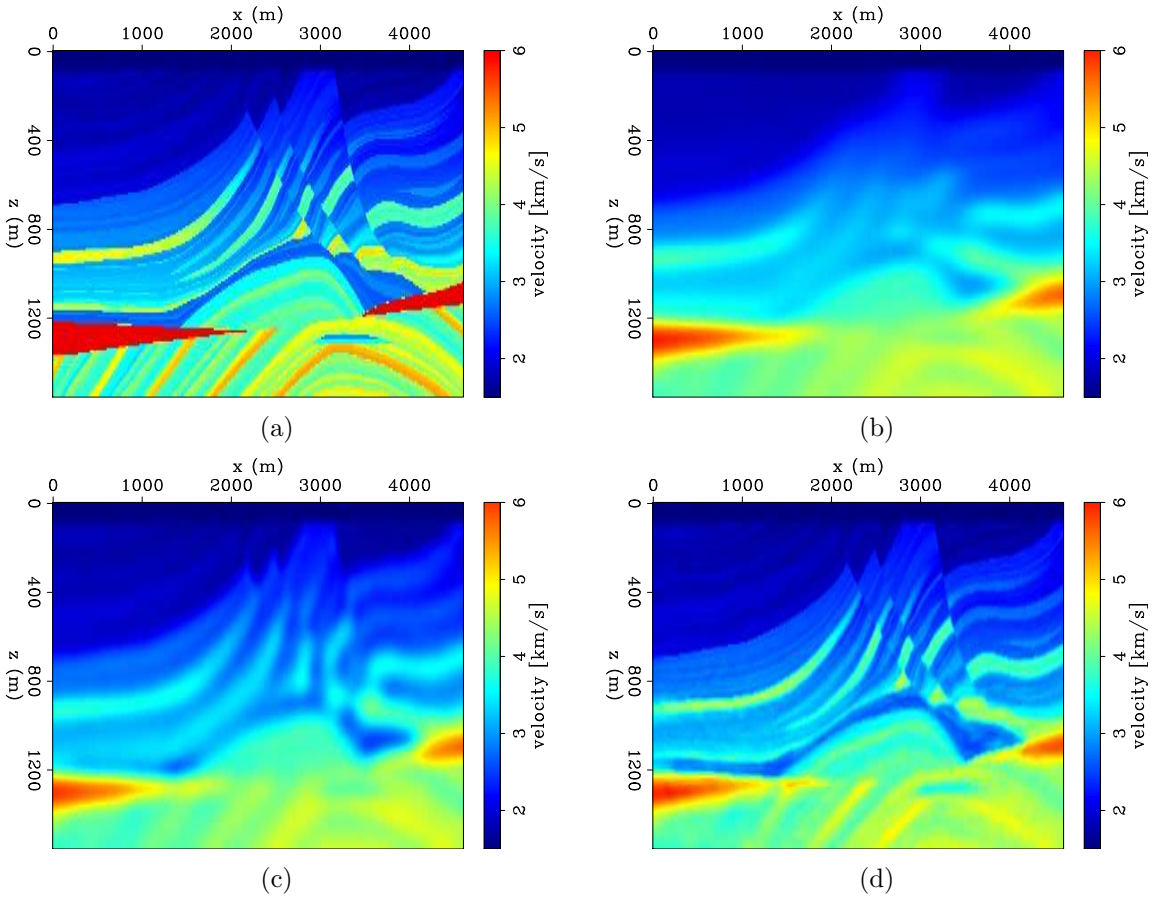

Figure 1: Panel (a) shows the true Marmousi velocity model. Panel (b) shows the initial Marmousi velocity model. Panel (c) shows the estimated velocity model using the data centered at 5 Hz. Panel (d) shows the estimated velocity model with the data centered at 30 Hz. [**CR**]

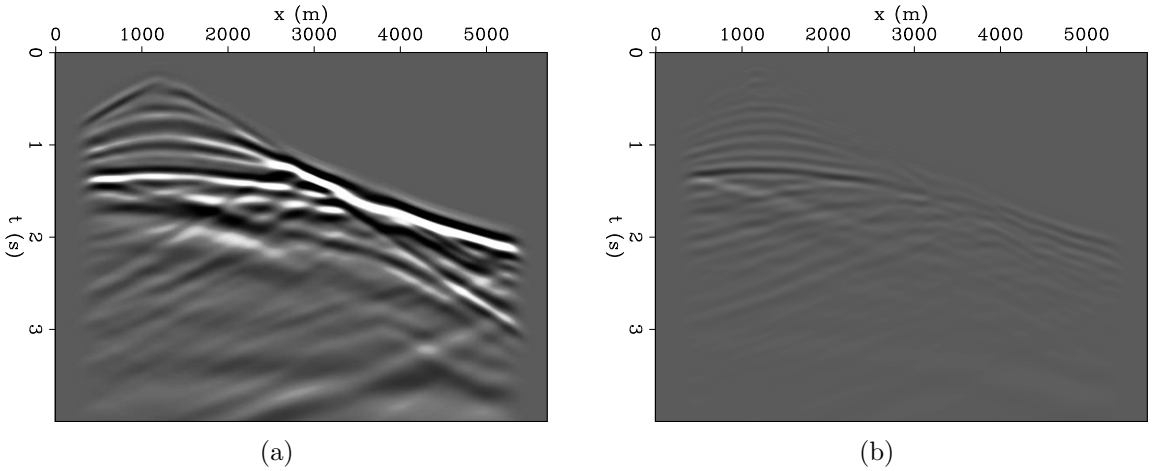

Figure 2: Panel (a) shows the data residual for the initial velocity model. Panel (b) show the data residual after FWI using the data centered at 5 Hz. [**CR**]

The effect of density on reflectivity will leak into the velocity model in the FWI workflow as shown in a previous study (Tang and Lee, 2015), thereby contaminating the inversion results. For the Marmousi model it is hard to identify the leakage visually because the density and the velocity model have a similar structures. Figure 3 shows the inversion results for velocity by forcing $\rho = 1$ in the FWI workflow.

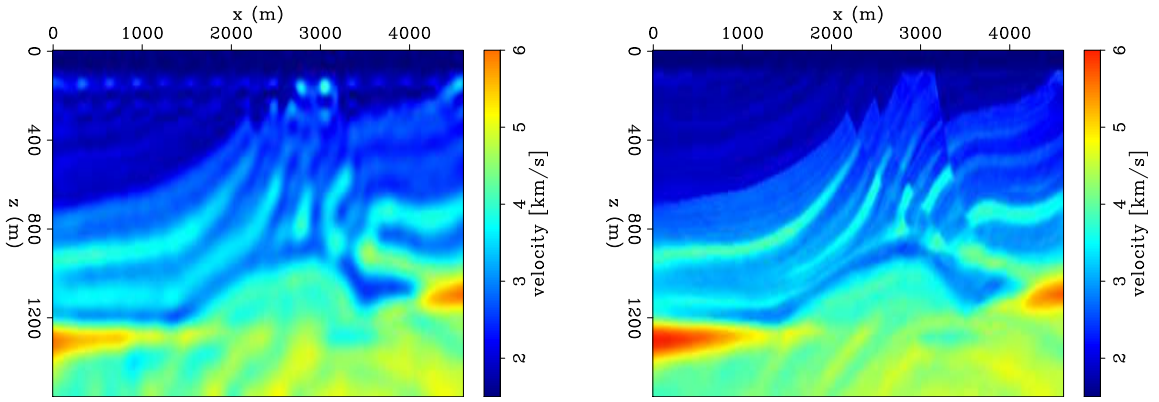

(a) (b)

Figure 3: Panel (a) shows the estimated Marmousi velocity model using using the data centered at 5 Hz, with $\rho = 1$. Panel (b) shows the estimated Marmousi density model after using the data centered at 30 Hz, with $\rho = 1$. [**CR**]

MULTIPARAMETER FULL-WAVEFORM INVERSION

Two acoustic parameters can be estimated for the wave Equation (2). First we estimate the velocity model and the density model simultaneously. The impedance I_p is obtained by multiplying velocity and density after the inversion. We can see the true models in Figures 4(a), 4(c) and 4(e). The initial models are shown in Figures 4(b) and 4(d). We start from data centered at 5 Hz to to avoid cycle skipping issues. The final inversion results are shown in Figures 5 using data centered at 30 Hz. The shallow area has been estimated properly except for the features below resolution because we use band-limited data. The lower left corner around $z = 1200\,m$ shows a clear crosstalk between velocity and density.

Once (m_v, m_ρ) has been estimated after inversion, we would like to know the feasibility of predicting acoustic impedance with Equation (24) as follows,

$$I_p = v\rho = v_0 e^{m_v} \times \rho_0 e^{m_\rho}. \tag{24}$$

Figure 5(c) shows the estimated impedance model using Equation (24). In this synthetic experiment, Equation (24) predicts the impedance model with high quality.

We also parameterize the wave equation using (m_v, m_{I_p}). The final inversion results are shown in Figure 6 after the same procedure shown in the (m_v, m_ρ) parameterization. The density model is computed by dividing the impedance model

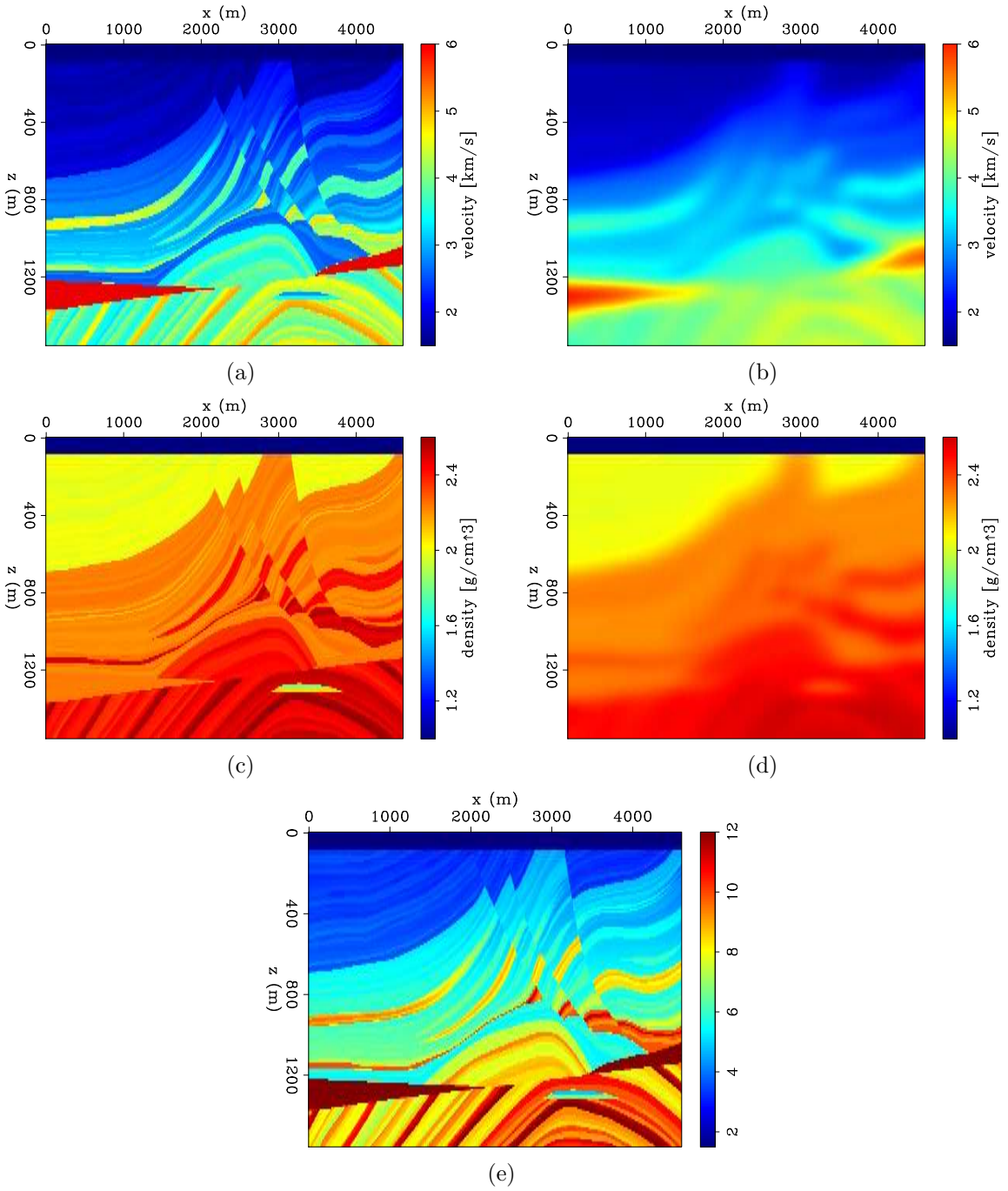

Figure 4: Panel (a) shows the true Marmousi velocity model. Panel (b) shows the initial Marmousi velocity model. Panel (c) shows the true Marmousi density model. Panel (d) shows the initial Marmousi density model. Panel (e) shows the true Marmousi impedance model. [**ER**]

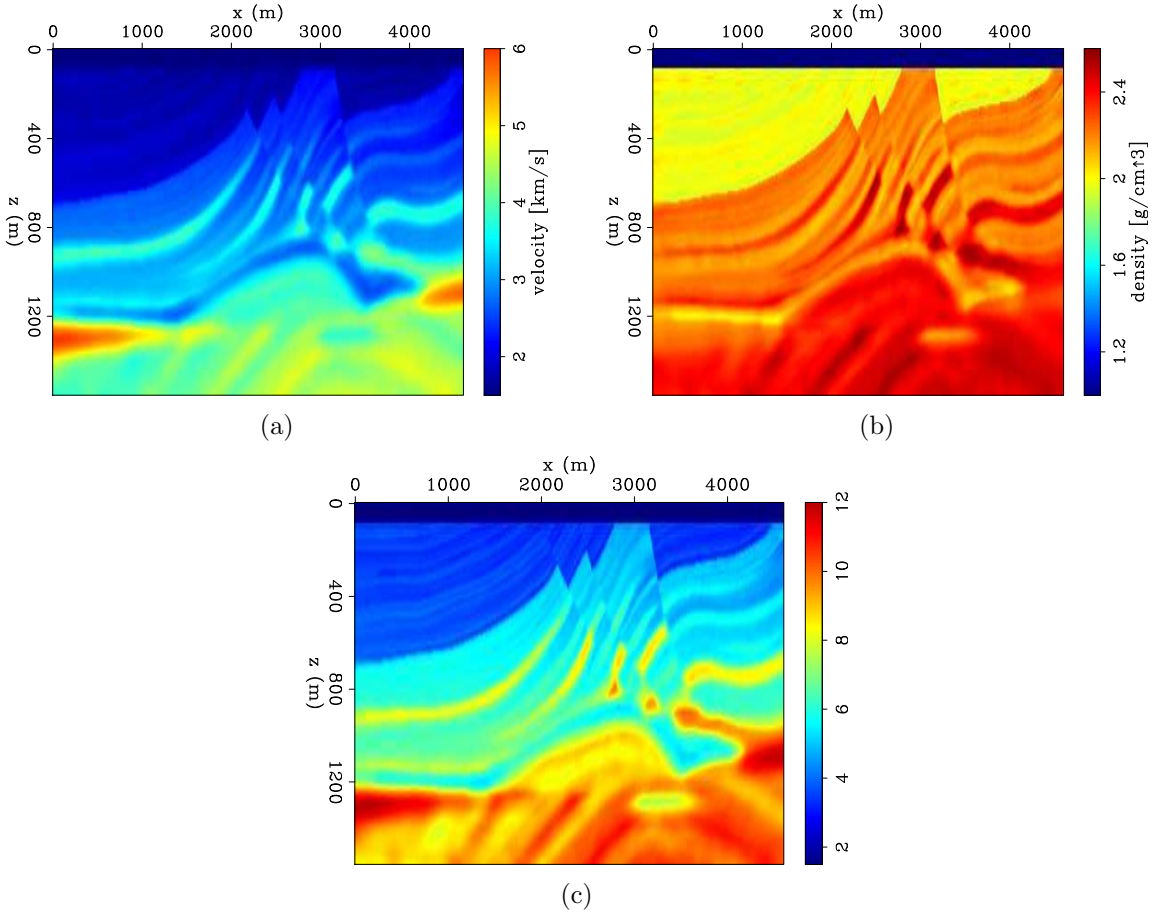

Figure 5: Panel (a) shows the estimated Marmousi velocity model using (m_v, m_ρ) parameterization. Panel (b) shows the estimated Marmousi density model using (m_v, m_ρ) parameterization. Panel (c) shows the estimated Marmousi impedance model by multiplying Panel (a) with Panel (b). [**CR**]

over the velocity model. The acoustic impedance is sensitivity to reflection seismic data because it controls reflectivity. Thereby the results in Figure 6 look sharper when compared with the results from (m_v, m_ρ) parameterization in Figure 5. The division may potentially damage the quality of the density model (Operto et al., 2013; Tang and Lee, 2015), because the velocity model and impedance model have different frequency content.

$$\rho = I_p/v = I_p e^{m_{I_p}} v_0^{-1} e^{-m_v}. \tag{25}$$

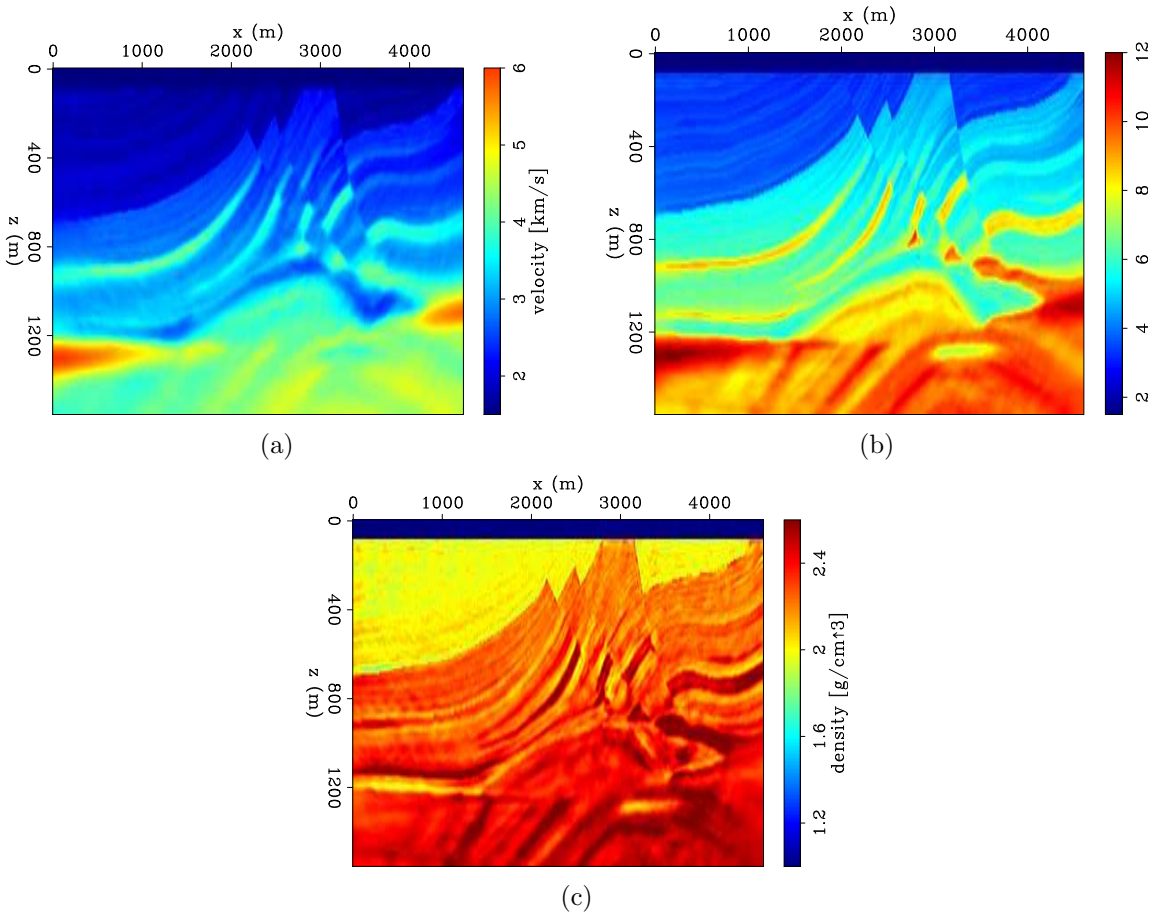

Figure 6: Panel (a) shows the estimated Marmousi velocity model using (m_v, m_{I_p}) parameterization. Panel (b) shows the estimated Marmousi impedance model using (m_v, m_{I_p}) parameterization. Panel (c) shows the estimated Marmousi density model by dividing Panel (b) over Panel (a). [**CR**]

REDUCING CROSSTALK USING THE HESSIAN

In this section, we study the crosstalk for different parameterizations and the feasibility of reducing the crosstalk using second-order methods.

We build a synthetic model with Gaussian perturbations. For (m_K, m_ρ) parameterization, the model perturbations are placed in a checkerboard pattern as shown in Figures 7(a) and 7(b). The gradients $\partial J/\partial m_K$ and $\partial J/\partial m_\rho$ have similar pattern with comparable amplitudes (in the opposite direction), as can be seen in Figures 7(c) and 7(d). This similarity is an indication that the off-diagonal components of the Hessian are as strong as the diagonal components. We apply the approximated inverse of the Hessian to the gradient, and the predicted model perturbations are shown in Figures 7(e) and 7(f). The crosstalk has been reduced significantly.

For (m_v, m_ρ) parameterization, the model perturbations and gradients are shown in Figure 8. The gradient for velocity $\partial J/\partial m_v$ has much higher amplitudes when compared with the gradient for density $\partial J/\partial m_\rho$. One can imagine that gradient based methods will have a slow convergence because the density model updates less compared with the velocity model for the first few iterations. We apply the approximated inverse of the Hessian to the gradient, and predict the model perturbations in Figures 8(e) and 8(f). The amplitudes for the predicted velocity perturbation and density perturbation are balanced.

We repeat the same procedure for the (m_v, m_{I_p}) parameterization, and the results are shown in Figure 9. We observe similar results as in the (m_v, m_ρ) parameterization.

CONCLUSIONS

We implemented multiparameter FWI in the acoustic media in this paper. We tested the FWI implementation on velocity estimation problem. FWI with different combinations of acoustic parameters were compared. Numerically, we found the (v, ρ) parameterization leads to smoother inversion results when compared with the (v, I_p) parameterization. The crosstalk between parameters for different parameterizations was studied. We showed that the crosstalk can be reduced by applying the inverse of the Hessian to the gradient.

REFERENCES

Alves, G., 2015, Adjoint formulation for the elastic wave equation : SEP Report 158.

Fichtner, A., 2011, Full Seismic Modeling and Inversion: Springer.

Fichtner, A. and J. Trampert, 2011, Hessian kernels of seismic data functionals based upon adjoint techniques: Geophysical Journal International, **185**, 775–798.

Maharramov, M. and B. Biondi, 2013, Simultaneous time-lapse full waveform inversion: SEP Report 150, 1–8.

Nocedal, J. and S. J. Wright, 2006, Numerical Optimization: Springer.

Operto, S., Y. Gholami, V. Prieux, a. Ribodetti, R. Brossier, L. Metivier, and J. Virieux, 2013, A guided tour of multiparameter full-waveform inversion with multicomponent data: From theory to practice: The Leading Edge, **32**, 1040–1054.

Plessix, R. E., 2006, A review of the adjoint-state method for computing the gradient

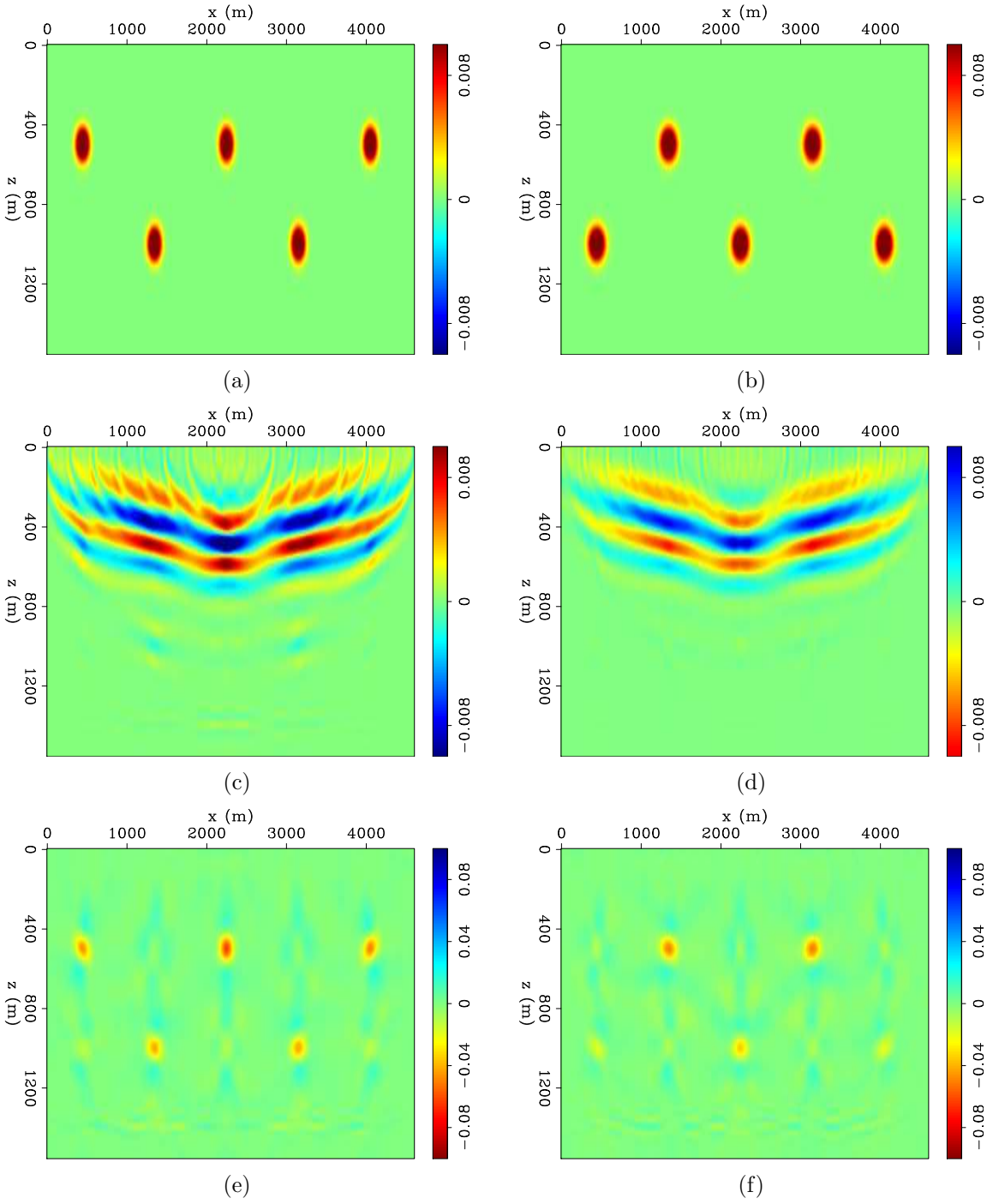

Figure 7: Panel (a) shows the bulk modulus perturbation. Panel (b) shows the density perturbation. Panel (c) shows the gradient for m_K. Panel (d) shows the gradient for m_ρ. Panel (e) shows the estimated bulk modulus perturbation by applying the approximated inverse of Hessian to the gradient. Panel (f) shows the estimated density perturbation by applying the approximated inverse of the Hessian to the gradient. [**CR**]

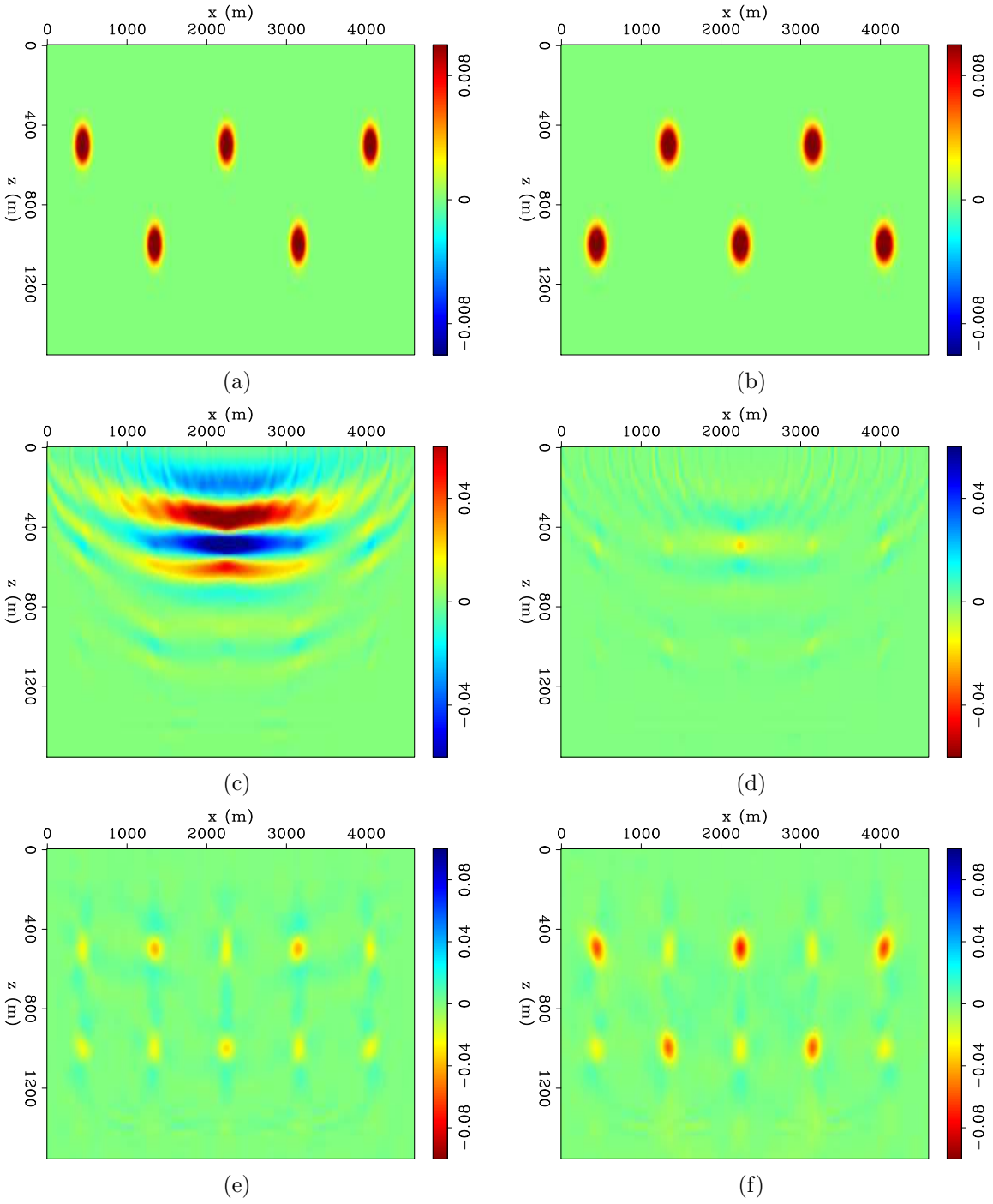

Figure 8: Panel (a) shows the velocity perturbation. Panel (b) shows the density perturbation. Panel (c) shows the gradient for m_v. Panel (d) shows the gradient for m_ρ. Panel (e) shows the estimated velocity perturbation by applying the approximated inverse of Hessian to the gradient. Panel (f) shows the estimated density perturbation by applying the approximated inverse of the Hessian to the gradient. [**CR**]

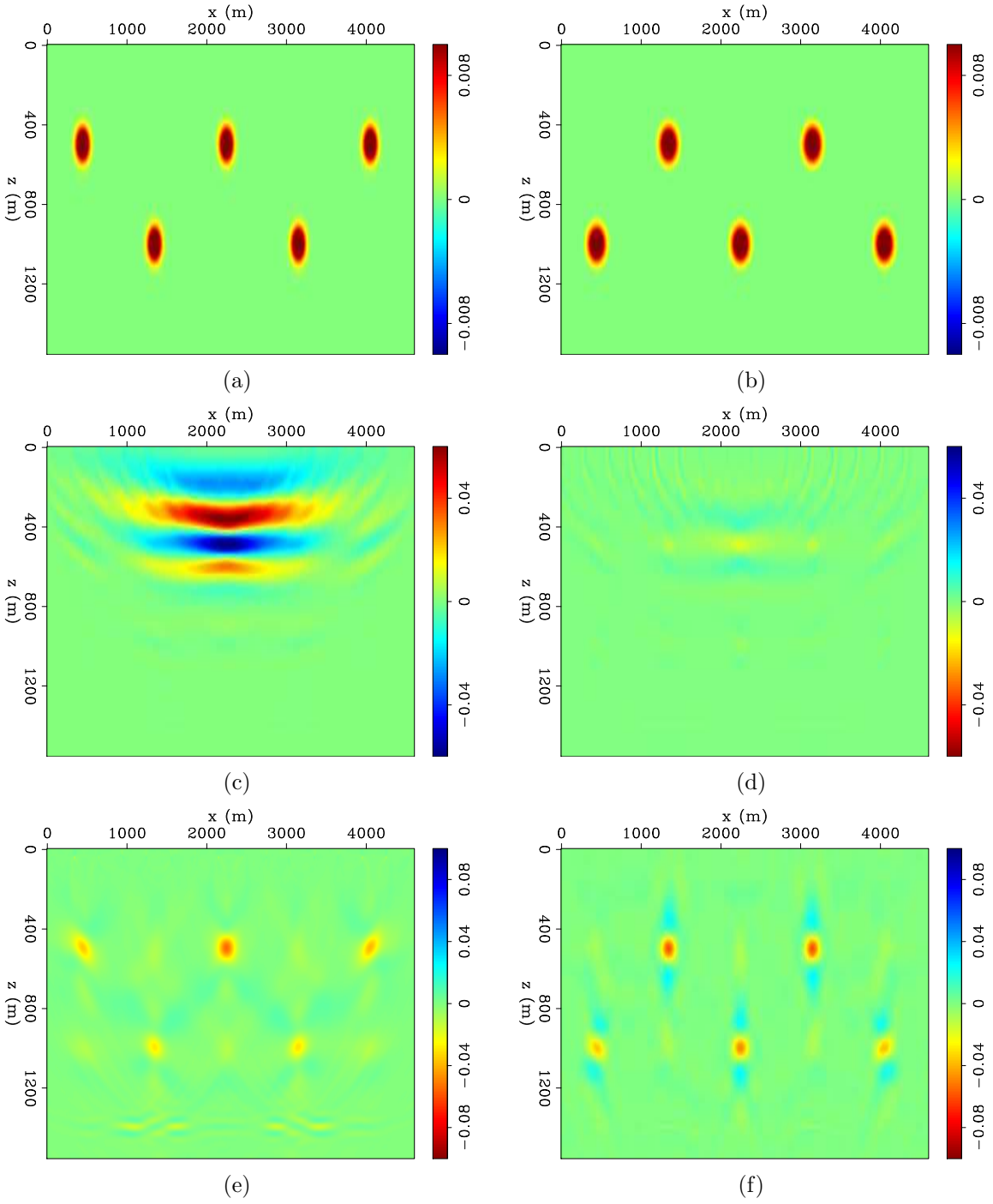

Figure 9: Panel (a) shows the velocity perturbation. Panel (b) shows the impedance perturbation. Panel (c) shows the gradient for m_v. Panel (d) shows the gradient for m_{I_p}. Panel (e) shows the estimated velocity perturbation by applying the approximated inverse of Hessian to the gradient. Panel (f) shows the estimated impedance perturbation by applying the approximated inverse of the Hessian to the gradient. [**CR**]

of a functional with geophysical applications: Geophysical Journal International, **167**, 495–503.

Tang, Y. and S. Lee, 2015, Multi-parameter full wavefield inversion using non-stationary point-spread functions: SEG Technical Program Expanded Abstracts 2015, 1111–1115.

Tarantola, A., 1984, in the Acoustic Approximation: Geophysics, **49**, 1259–1266.

Tromp, J., C. Tape, and Q. Liu, 2005, Seismic tomography, adjoint methods, time reversal and banana-doughnut kernels: Geophysical Journal International, **160**, 195–216.

Virieux, J. and S. Operto, 2009, An overview of full-waveform inversion in exploration geophysics: Geophysics, **74**, WCC1.